Geophysical Research Letters

RESEARCH LETTER
10.1029/2020GL088335

A Mechanism for the Arctic Sea Ice Spring Predictability Barrier

Mitchell Bushuk[1,2], Michael Winton[1], David B. Bonan[3], Edward Blanchard-Wrigglesworth[4], and Thomas L. Delworth[1]

[1]Geophysical Fluid Dynamics Laboratory, NOAA, Princeton, NJ, USA, [2]University Corporation for Atmospheric Research, Boulder, CO, USA, [3]Environmental Science and Engineering, California Institute of Technology, Pasadena, CA, USA, [4]Department of Atmospheric Sciences, University of Washington, Seattle, WA, USA

Key Points:
- The Arctic sea ice spring predictability barrier is investigated using a daily mass budget analysis
- A mechanism for the spring predictability barrier is proposed, involving three distinct predictability regimes
- The spring barrier is expected to shift earlier under Arctic warming due to shifts in melt onset timing

Supporting Information:
- Supporting Information S1

Correspondence to:
M. Bushuk,
mitchell.bushuk@noaa.gov

Citation:
Bushuk, M., Winton, M., Bonan, D. B., Blanchard-Wrigglesworth, E., & Delworth, T. L. (2020). A mechanism for the Arctic sea ice spring predictability barrier. *Geophysical Research Letters*, *47*, e2020GL088335. https://doi.org/10.1029/2020GL088335

Received 8 APR 2020
Accepted 21 MAY 2020
Accepted article online 9 JUN 2020

Abstract The decline of Arctic sea ice extent has created a pressing need for accurate seasonal predictions of regional summer sea ice. Recent work has shown evidence for an Arctic sea ice spring predictability barrier, which may impose a sharp limit on regional forecasts initialized prior to spring. However, the physical mechanism for this barrier has remained elusive. In this work, we perform a daily sea ice mass (SIM) budget analysis in large ensemble experiments from two global climate models to investigate the mechanisms that underpin the spring predictability barrier. We find that predictability is limited in winter months by synoptically driven SIM export and negative feedbacks from sea ice growth. The spring barrier results from a sharp increase in predictability at melt onset, when ice-albedo feedbacks act to enhance and persist the preexisting export-generated mass anomaly. These results imply that ice thickness observations collected after melt onset are particularly critical for summer Arctic sea ice predictions.

Plain Language Summary Observations over the past 40 years have documented a significant decline in Arctic sea ice extent and thickness. These rapid changes and their implications for Northern communities, shipping industries, wildlife, fisheries, and natural resource industries have created an emerging operational need for regional summer sea ice predictions. This study is motivated by the following question: How far in advance can accurate predictions of regional summer sea ice be made? Recent work has shown evidence for an Arctic sea ice spring predictability barrier, which may fundamentally limit the accuracy of predictions made before May. However, the physical mechanism for this barrier has remained elusive. In this study, we investigate this mechanism using a sea ice mass (SIM) budget analysis, which allows for a process-based attribution of summer sea ice predictability. We considerthe relative roles of ice growth and melt (thermodynamics) and ice motion (dynamics) in determining the spring predictability barrier. We find that predictability is limited by ice motion and growth in winter and increases rapidly in spring due to melt processes. These results imply that ice thickness observations collected after spring melt onset are particularly critical for summer Arctic sea ice predictions.

1. Introduction

The observed decline of summer Arctic sea ice extent (Cavalieri & Parkinson, 2012) and thickness (Kwok, 2018) has created a host of new opportunities and challenges associated with operating in the "New Arctic." These future operations will rely upon accurate prediction of regional sea ice across a range of timescales spanning from hours to seasons (Jung et al., 2016). The potential advancement of Arctic sea ice prediction capability is underpinned by a crucial question: How far in advance can skillful predictions of regional summer sea ice be made? In this study, we argue for the existence of an *Arctic sea ice spring predictability barrier*, which imposes a relatively sharp limit on regional summer sea ice prediction skill.

A number of recent studies have shown evidence for an Arctic sea ice spring predictability barrier—defined as a springtime date such that predictions initialized on or after the date can skillfully predict summer sea ice, whereas predictions initialized prior to the date have much lower skill. Day, Tietsche, et al. (2014) was the first study to introduce the concept of a spring predictability barrier for Arctic sea ice. They showed using HadGEM1.2 perfect model experiments—which define the upper limits of predictability in a particular model—that predictions of pan-Arctic and regional sea ice extent (SIE) initialized on 1 May lost skill more rapidly than those initialized on 1 July. Melia et al. (2017) explored the same suite of experiments

and showed evidence for a May predictability barrier for shipping routes along Eurasia's Northern Sea Route, which traverses the Chukchi, East Siberian, Laptev, Kara, and Barents Seas. Bushuk et al. (2017a) showed the existence of a spring predictability barrier in initialized dynamical seasonal forecasts of observed SIE in the Laptev, East Siberian, and Beaufort Seas. Using perfect model experiments performed with the same Geophysical Fluid Dynamics Laboratory Forecast-oriented Low Ocean Resolution (GFDL-FLOR) dynamical model, Bushuk et al. (2018) showed that the same regional SIE spring predictability barrier was also present in the perfect model context, suggesting that the spring barrier was a fundamental predictability feature of this model.

Bonan et al. (2019) extended these initial results to a broader suite of fully coupled global climate models (GCMs), showing that a spring predictability barrier for regional Arctic sea ice area (SIA) was a robust feature across nearly all GCMs participating in Phase 5 of the Coupled Model Intercomparison Project (CMIP5). They showed some intermodel spread in the timing of the predictability barrier but found that most GCMs had a common barrier date between 1 May and 1 June. This barrier timing aligns with the period of rapid spring sea ice error growth identified by earlier perfect model studies (Blanchard-Wrigglesworth, Bitz, et al., 2011; Holland et al., 2011; Tietsche et al., 2014), suggesting that ice-albedo feedbacks may be a crucial element of the spring barrier. Both Day, Tietsche, et al. (2014) and Bonan et al. (2019) found that while pan-Arctic SIA predictions had some barrier-like characteristics, the barrier was defined much more sharply for regional sea ice predictions.

Statistical prediction methods, based purely on observed quantities, also show evidence of a spring predictability barrier. The study of Brunette et al. (2019), which used winter coastal divergence as a predictor of summer Laptev SIE, found maximum skill when coastal divergence was integrated up to the first week of May and a notable drop in skill when integrated to the first week of April. Other statistical prediction systems report skillful detrended SIE predictions for forecasts initialized after 1 May, but not prior to this date, consistent with a spring predictability barrier (Kapsch et al., 2014; Lindsay et al., 2008; Liu et al., 2015; Petty et al., 2017; Schröder et al., 2014; Walsh et al., 2019; Williams et al., 2016; Yuan et al., 2016). Similarly, while not necessarily mentioning a spring barrier, other studies documenting the detrended Arctic SIE prediction skill of dynamical prediction systems display a barrier-like skill structure corresponding to initialization month May (Dirkson et al., 2019; Merryfield et al., 2013; Msadek et al., 2014; Sigmond et al., 2013; Wang et al., 2013).

While these studies represent a growing body of evidence for the existence of a regional Arctic sea ice spring predictability barrier, the physical mechanism responsible for the barrier has remained elusive. In this work, we seek to provide a mechanism for the spring barrier. We perform a sea ice mass (SIM) budget analysis using daily data from large ensemble experiments performed with two different GCMs. This analysis allows for a process-based attribution of summer sea ice predictability, revealing a mechanism for the spring predictability barrier. We then consider the evolution of the predictability barrier under climate change and the implications of these results for future seasonal prediction systems.

2. Methods

2.1. Large Ensemble Simulations

We consider two suites of large ensemble experiments performed with the Community Earth System Model Version 1 using the Community Atmosphere Model version 5 (CESM1 (CAM5); Hurrell et al., 2013) and the GFDL-FLOR model (Vecchi et al., 2014), respectively. The CESM Large Ensemble (CESM-LE; Kay et al., 2015) is a 40-member ensemble that uses historical radiative forcings from 1920–2005 and representative concentration pathway 8.5 (RCP8.5; Meinshausen et al., 2011) from 2006–2100. The initial conditions for the CESM-LE are nearly identical, differing only by roundoff-level perturbations in their atmospheric initial states. The FLOR Large Ensemble (FLOR-LE) is a 30-member ensemble spanning 1921–2100 and also uses historical and RCP8.5 radiative forcings. The FLOR-LE members were initialized using climate states from an 1,160-year preindustrial control run of FLOR. The initial conditions were taken every 10 years from simulation years 821–1,111, in order to sample different phases of internal decadal climate variability.

The CESM1(CAM5) has a nominal horizontal resolution of 1° in all model components with 60 vertical ocean levels and 30 vertical atmospheric levels (Hurrell et al., 2013; Kay et al., 2015). The sea ice

component of CESM1 is primarily based on Version 4 of the Los Alamos National Laboratory (LANL) Community Ice Code (CICE4; Hunke et al., 2008). This model uses an elastic-viscous-plastic (EVP) rheology to solve for internal ice stresses (Hunke & Dukowicz, 2002), a five-category subgrid-scale ice thickness distribution (ITD; Thorndike et al., 1975; Bitz et al., 2001), energy-conserving thermodynamics (Bitz & Lipscomb, 1999), a delta-Eddington shortwave radiation scheme (Briegleb & Light, 2007), and the associated capability to explicitly simulate sea ice melt ponds (Holland et al., 2012). FLOR has nominal horizontal resolutions of 1° in the sea ice and ocean components and 0.5° in the atmosphere and land components, with 50 vertical ocean levels and 32 vertical atmospheric levels (Vecchi et al., 2014). FLOR's sea ice component is the Sea Ice Simulator Version 1 (SIS1; Delworth et al., 2006), which, similar to CESM1, employs an EVP rheology for sea ice dynamics and a five-category ITD. SIS1 uses a modified Semtner three-layer thermodynamic scheme with two ice layers and one snow layer (Winton, 2000) and parameterizes the effects of melt ponds using an albedo formulation based on surface temperature (see section 3.6.2 of Hunke et al., 2015).

We assess these simulations using daily passive microwave sea ice concentration (SIC) observations from the National Snow and Ice Data Center (NSIDC) processed using the NASA Team Algorithm (Data Set ID: NSIDC-0051; Cavalieri et al., 1996). We also use daily sea ice thickness (SIT) data from the Pan-Arctic Ice Ocean Modeling and Assimilation System (PIOMAS; Zhang & Rothrock, 2003). PIOMAS is an ice-ocean reanalysis product that compares reasonably well to available satellite, aircraft, and in situ SIT measurements (Schweiger et al., 2011; Wang et al., 2016).

2.2. SIM Budget Analysis and Covariance Decomposition

The overall strategy for this study of the predictability barrier mechanism is described here. Following Bonan et al. (2019), we characterize the predictability barrier via lagged correlation between SIA at a given target day t, A_t, and SIM at a lead time of τ days, $M_{t-\tau}$. These correlations are the prediction skill of a linear regression forecast based on regional SIM and are close to the upper limit of predictability as estimated by perfect model experiments (Bonan et al., 2019). We seek a process-based attribution of the SIA-SIM correlation structure by performing an SIM budget analysis. A useful route to understanding these lagged correlations is via the SIA-SIM covariance, which is the numerator of the correlation coefficient. The advantage of considering the SIA-SIM covariance is that it can be linearly decomposed into contributions from the various mass budget components. We can then assess the predictability contributions from each mass budget term, focusing on their relationship to the spring predictability barrier.

Our SIM budget analysis is performed with daily temporal resolution using the mass budget diagnostics that were saved in both the CESM-LE and FLOR-LE experiments. In both models, the SIM at each grid cell evolves according to the following equation:

$$\frac{\partial}{\partial t}M(t) = GROWTH(t) + MELT(t) + XPRT(t), \tag{1}$$

where the source terms are mass fluxes (in units of $\mathrm{kg\,m^{-2}\,s^{-1}}$) associated with sea ice growth, melt, and mass transport convergence (henceforth, export), respectively. The melt and growth terms result from thermodynamic processes, whereas the export term results from dynamic processes. The melt term comprises top, basal, and side melt and the growth term comprises both basal and frazil ice growth. The melt and growth terms also include contributions from snow-to-ice conversion, evaporation, and sublimation, but these contributions are small compared with other terms in the mass budget (e.g., Keen et al., 2020). Positive export values indicate mass convergence and negative values indicate mass divergence. Note that the FLOR mass budget diagnostics include the mass of snow on sea ice. The contribution of snow mass to $M(t)$ is relatively modest, ranging from approximately 5% in winter and spring to less than 1% in summer. Additionally, SIM time series computed directly as the product of SIC, SIT, and sea ice density share very similar variability with the $M(t)$ time series (note that sea ice density has a constant value of $905\,\mathrm{kg/m^3}$ in FLOR and SIT is the thickness in the ice-covered portion of the grid cell).

By temporally integrating Equation 1 from time t_0 to t, we can reconstruct the contributions of the three budget components to a given SIM state. Decomposing the mass flux terms into climatological and anomalous contributions, we recover the decomposed mass time series

$$M(t) = \langle M(t) \rangle + M'_{GROWTH}(t) + M'_{MELT}(t) + M'_{XPRT}(t) + M'(t_0), \quad (2)$$

where $\langle M(t) \rangle$ is the ensemble mean seasonally varying mass climatology, $'$ symbols indicate anomalies, and $M'(t_0)$ is the initial mass anomaly at time t_0.

We consider summer SIA predictability via the SIA-SIM covariance, $C(A'_t, M'_{t-\tau})$. Using the mass budget decomposition in Equation 2 and the linearity of the covariance function C, we have that

$$C(A'_t, M'_{t-\tau}) = C(A'_t, M'_{GROWTH,t-\tau}) + C(A'_t, M'_{MELT,t-\tau}) + C(A'_t, M'_{XPRT,t-\tau}) + C(A'_t, M'_{t_0}). \quad (3)$$

This decomposition allows us to assess the contribution that each of the mass budget terms makes to the covariance with SIA.

2.3. Climate Epoch Analysis

To analyze the influence of a shifting climate mean state on the predictability barrier, we consider the LE data in different temporal "epochs," defined as 10-year periods centered upon a given year. The CESM and FLOR-LEs provide 400 and 300 realizations within each epoch, respectively, allowing us to simultaneously compute robust statistics while probing relatively narrowly defined climate mean states. We consider anomalies defined relative to the time-evolving ensemble mean. We also consider a "control epoch" centered upon 1990 (1986–1995), which is in the satellite era and just prior to the period of rapid sea ice decline. Our analysis is based on Arctic regional-mean quantities, using the regional definitions of Bushuk et al. (2017a) (see Figure S1 in the supporting information).

3. Results

3.1. Spring Predictability Barrier in CESM and FLOR

We begin by documenting the predictability barrier structure in the control epoch of the CESM-LE and FLOR-LE. We focus on the Laptev Sea in the forthcoming figures, but the same qualitative conclusions hold for the other dominant regions of summer Arctic sea ice variability. These other regions are presented in the supporting information (Figures S1–S7) and discussed ahead.

Figures 1a and 1b show the climatology of regional-mean SIC and SIT in the Laptev Sea in the control epoch. Both models reproduce the observed seasonal cycle of SIC reasonably well but share a common high bias of 2–10% throughout the year ($0.015–0.07 \times 10^6$ km^2). The high wintertime SIC bias is notable, suggesting that both models have too low a propensity to open leads in highly compact sea ice. This high winter SIC bias is similarly present in all peripheral seas of the Arctic basin (Figure S2). The models' regional SIT climatologies generally bracket those of PIOMAS, with CESM being thicker and FLOR being thinner.

Figures 1c and 1d show the climatology of mass budget terms in the Laptev Sea. We find a high degree of agreement between CESM and FLOR, both in the magnitude of mass budget terms and the shape of their seasonal cycles. Both models thermodynamically grow ice at a rate of roughly 4 m/year between 1 November and 1 March and have a maximum summer melt rate of roughly 9 m/year. We define melt onset as the date when melt rates first exceed 1 m/year, which agrees well with a surface-temperature-based definition of melt onset (not shown). FLOR's melt onset date of 20 May is 2 weeks earlier than the 3 June melt onset of CESM, similar to the models' gap in timing of maximum summer melt. The mass export climatology is notably noisier than the thermodynamic terms, reflecting the impact of high-frequency (daily-to-weekly) atmospheric variability on sea ice export. Both models export ice out of the Laptev Sea domain in the winter months, consistent with wind-driven coastal divergence associated with storms (e.g., Brunette et al., 2019; Krumpen et al., 2013; Preußer et al., 2016; Willmes et al., 2011). Both models import ice in the summer months, with the greater import rates in CESM possibly related to its greater mean thickness in the Central Arctic. The mass budget climatologies in other Arctic regions share a similar degree of consistency (Figure S3).

Figures 1e and 1f show Laptev Sea lagged correlations between daily SIA and earlier SIM up to lead times of 364 days (i.e., the prediction skill of a linear regression forecast using regional SIM as a predictor). Both CESM and FLOR display a clear diagonal correlation structure, similar to those found in Bonan et al. (2019) using monthly CMIP5 data. For all summer target dates (1 June to 1 October), we find that

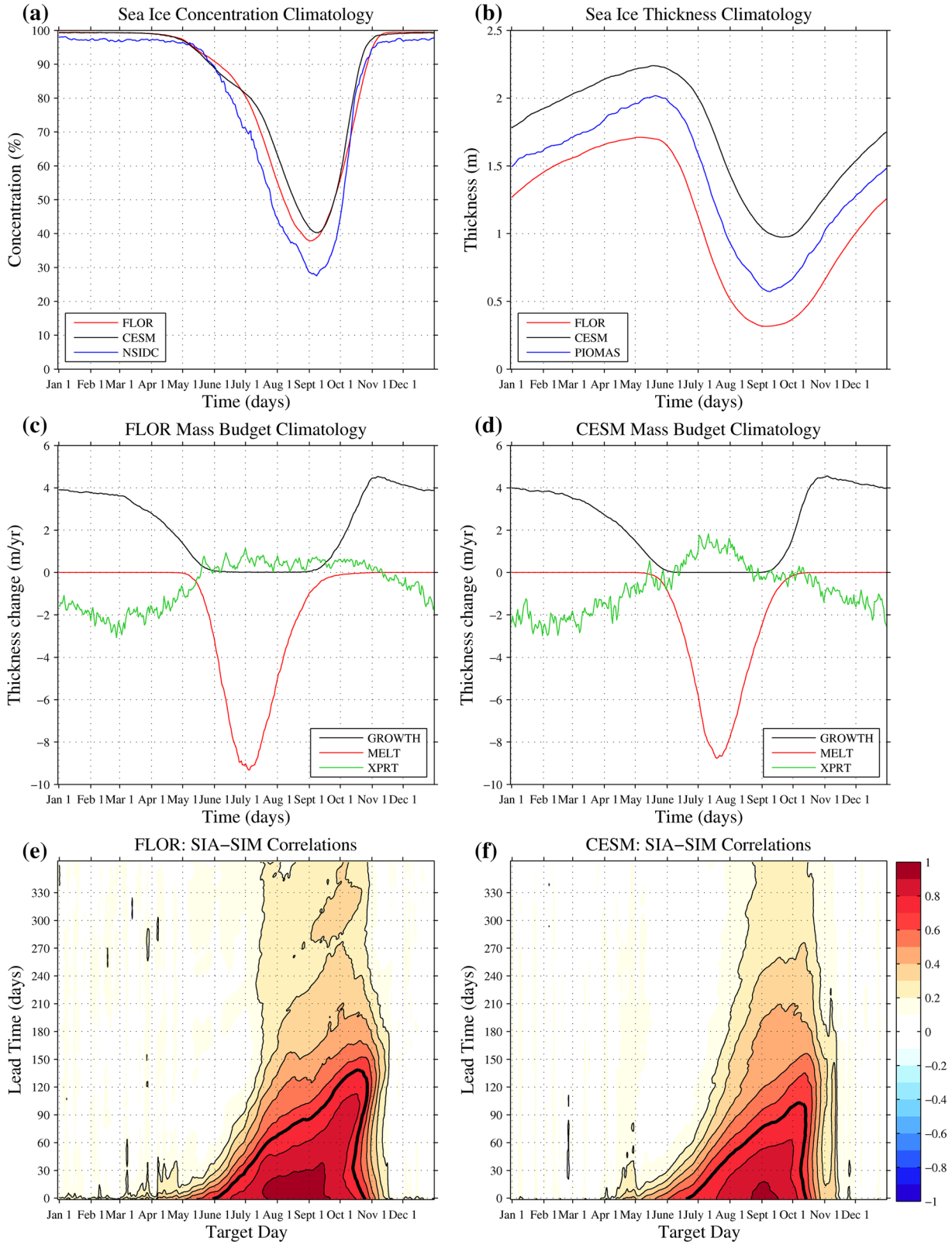

Figure 1. Laptev Sea control epoch climatology and predictability barrier in FLOR and CESM. (a, b) SIC and SIT climatologies in FLOR (red) and CESM (black) compared to NSIDC observations and PIOMAS reanalysis (blue). The NSIDC and PIOMAS climatologies are computed over 1981–2000. (c, d) Mass budget climatologies showing growth (black), melt (red), and export (green) rates. (e, f) Lagged correlations between SIA and earlier SIM. The thick black contours indicate $r = 0.7$.

correlation values tend to drop off at a fixed initialization date. We compute a "barrier date" by finding the date at which prediction skill drops most rapidly (computed as the squared decorrelation) for each target date, and averaging over all summer target dates. This barrier date is 31 May in FLOR and 12 June in CESM, which correspond closely to the $r = 0.7$ contours in Figures 1e and 1f. This difference in barrier date is similar to the models' differences in climatological timing of melt onset. Lagged correlations for other Arctic regions also display a spring predictability barrier; however, there are regional differences in the details of their correlation structures (Figure S4). Lagged correlations between summer SIM and earlier SIM are generally higher than the SIA-SIM correlations, owing partially to persistence of SIM anomalies in the multiyear ice pack that do not couple strongly with summer SIA (Figure S5).

3.2. A Mechanism for the Spring Predictability Barrier

Since long-lead correlations between regional SIM and SIA are quite weak ($r<0.3$ for lead >330 days), we focus on the development of SIM anomalies from 1 October through to the following summer. To build intuition, we first consider the development of SIM anomalies in individual high-mass years from each model (Figures 2a and 2b). The SIM anomaly time series (magenta curves) each display an overall development of positive anomalies that peak over the summer months and are punctuated by high-frequency variability on daily-to-weekly timescales. Following the positive summer SIM anomaly, we find a corresponding positive anomaly in late summer SIA, as expected from Figures 1e and 1f. The individual mass budget terms make distinct contributions to this overall anomaly and are qualitatively similar between the models.

The growth term (black curves) generally acts to oppose the positive SIM anomaly, consistent with the negative feedback between ice growth rates and ice thickness (Bitz & Roe, 2004; Massonnet et al., 2018). This suggests that the growth term is not the primary driver of SIM anomalies and rather responds as a negative feedback to anomalies produced via other mass budget terms. The strength of this negative feedback is given by the instantaneous slope of the growth curve, which mirrors the instantaneous SIM anomaly (e.g., Figure 2a shows a strong negative feedback in January associated with large SIM anomalies and a weaker negative feedback in February associated with smaller SIM anomalies). In both models, the export term (green curves) is the clear driver of daily-to-weekly SIM variability, showing the dominant role of synoptic atmospheric variability in driving ice dynamics and regional mass variations (cf. Figure A4 of Blanchard-Wrigglesworth & Bitz, 2014). These high-frequency fluctuations accumulate over the fall, winter, and spring months, resembling a random walk, and eventually result in a positive SIM anomaly in mid-May. The initial SIM anomaly also contributes to this mid-May anomaly; however, in the absence of ice export, this contribution is relatively modest. This can be roughly visualized by the growth terms in Figures 2a and 2b, which act to reduce the initial anomaly to a fairly small positive anomaly by mid-May. The melt term (red curves) becomes active in mid-May in FLOR and early June in CESM. This term provides a positive feedback, acting to further amplify the preexisting positive SIM anomaly. This positive feedback is consistent with ice-albedo feedbacks that occur in late spring and early summer associated with both top melt and basal melt (e.g., Curry et al., 1995). The mass budget terms have a qualitatively similar behavior, with opposite sign, in low-mass years (Figures 2c and 2d).

Figure 2 is suggestive of a mechanism for the spring predictability barrier. In particular, the dominant control on winter SIM variability is export, which is likely driven by high-frequency wind forcing that is unpredictable beyond a few weeks. SIM acts as an integrator of this nearly white noise forcing, producing anomalies that are opposed by negative feedbacks from sea ice growth. This combination of unpredictable high-frequency forcing and the negative growth thickness feedback lead to SIM anomalies that have relatively low predictability beyond a few months during the winter. However, the particular SIM anomaly that is present in mid-May will be "locked in" at melt onset via positive ice-albedo feedbacks, owing to predictable changes in top and basal melt, which cause the preexisting anomaly to grow. This SIM anomaly persists to late summer, creating a corresponding anomaly in SIA.

We assess this proposed mechanism using the covariance decomposition of Equation 3. This linear decomposition allows us to evaluate the individual contributions of each mass budget term to the covariance between SIA and earlier SIM. In Figure 3, we plot this decomposition for a 1 September SIA target date and different initialization dates. The mass budget terms are accumulated from the previous 1 October, and covariances with 1 September SIA are computed at each initialization date.

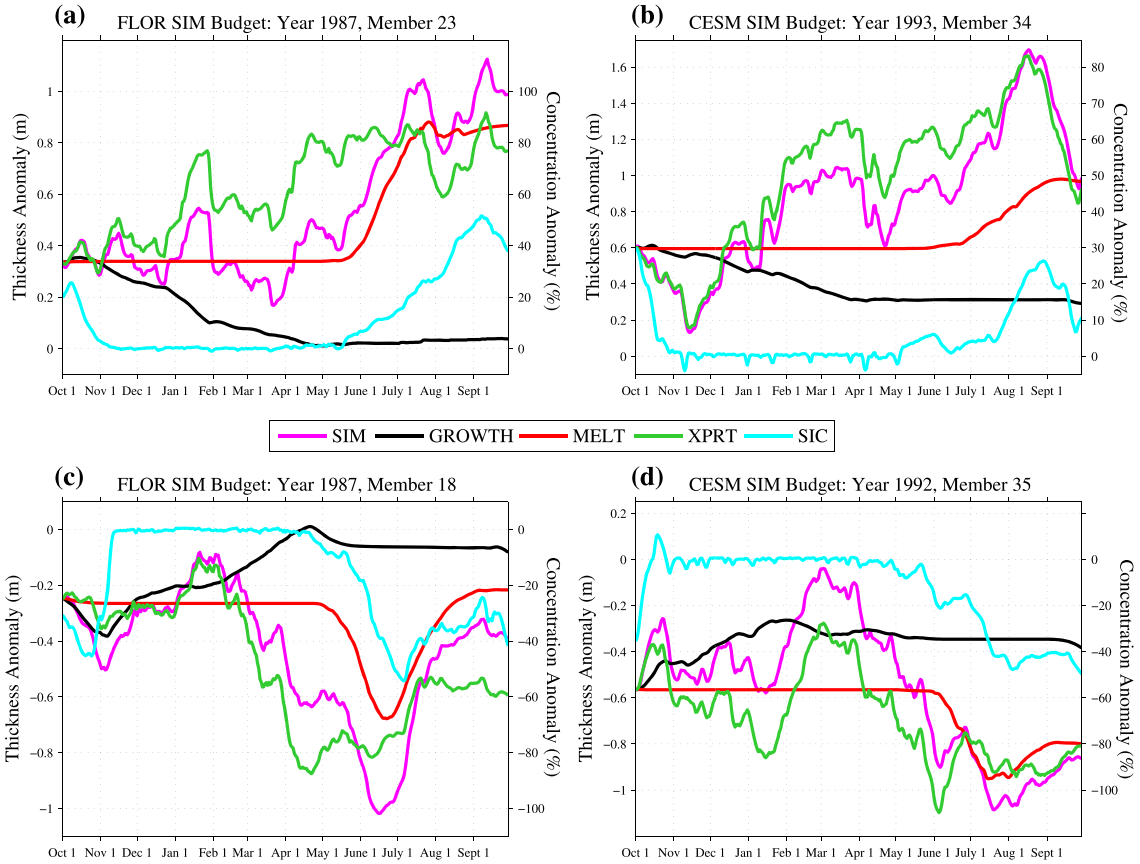

Figure 2. Mass budget decomposition in FLOR and CESM in individual high mass (a, b) and low mass (c, d) years in the Laptev Sea. Plotted are the evolution of full SIM anomalies (magenta) and the accumulated contributions from the growth (black), melt (red), and export (green) terms beginning from 1 October. The accumulated contributions are plotted relative to the initial 1 October SIM value. SIC anomalies are plotted in cyan.

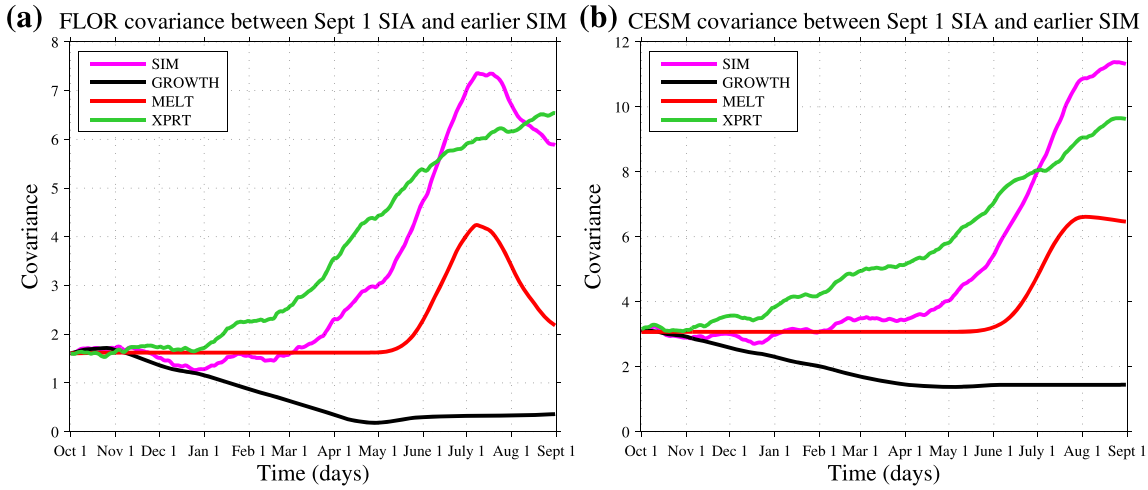

Figure 3. Covariance decomposition between 1 September SIA and earlier SIM in FLOR (a) and CESM (b) in the Laptev Sea in the control epoch. The mass budget terms are accumulated from the previous 1 October, and covariances with 1 September SIA are computed at each initialization date. Plotted are the full SIM covariance (magenta) and the covariance contributions from the growth (black), melt (red), and export (green) terms. Covariance contributions are plotted relative to the initial 1 October SIM covariance.

In both models, 1 September SIA anomalies positively covary with SIM anomalies on the previous 1 October (magenta curves), indicating some year-to-year persistence of regional mass anomalies. However, these covariance values are roughly 25% of the maximum covariance achieved at shorter lead times, suggesting that year-to-year SIM persistence is not the dominant source of predictibility for summer SIA. The SIM covariances display sharp increases in mid-May in FLOR and early June in CESM. These sharp increases are the signature of the predictability barrier, as they indicate the timing at which forecasts benefit substantially from a slightly later initialization date.

We find that the dominant contribution to SIM covariance comes from the export term, which increases monotonically as the initialization date approaches 1 September (green curves). In both models, the export-driven covariance contributions are relatively flat until roughly 1 January, at which point they start to increase. Interestingly, in their observation-based analysis, Brunette et al. (2019) also identified early January as a critical time when export-driven anomalies begin increasing. The export-driven covariance increases roughly linearly in CESM and sublinearly in FLOR. Crucially, neither model shows a spring barrier-like feature associated with export. The growth term (black curves) provides a negative feedback on the export-driven anomalies, acting to reduce the positive covariance between wintertime SIM and September SIA. This feedback is particularly active between 1 November and 1 April, limiting the degree to which export is able to generate predictive SIM anomalies. Finally, we find that the melt-driven covariance (red curves) increases sharply in mid-May in FLOR and early June in CESM and is responsible for driving the rapid increase in SIM covariance at these times. This shows that melt processes provide the critical increase in spring SIM covariance that underpins the predictability barrier. The melt-based covariance terms become active at the timing of melt onset, implying that melt onset provides an important control on the timing of the spring barrier. Indeed, FLOR's barrier date is roughly 2 weeks earlier than CESM's, consistent with their climatological differences in melt onset (Figures 1c–1f). We note that FLOR's SIM-SIA covariance decreases after mid-July. This is due to an areal effect. For example, low SIM years are nearly ice-free in late summer. With less ice area available to melt, this leads to less total melt (a positive mass anomaly), which acts in the opposite direction of the mass anomaly produced via positive feedbacks in May–July. A less pronounced version of this effect is also present in CESM. Note that covariances computed using the melt per unit ice area increase continuously up to 1 September (not shown).

Figure 3 suggests the existence of three distinct predictability regimes for summer sea ice predictions. The first regime, occurring during the period of high sea ice growth and strong negative feedback from roughly 1 October to 1 April, is characterized by relatively modest increases in SIM-based predictability. The second regime, from roughly 1 April to melt onset, has larger increases in predictability due to lower ice growth rates and a weaker negative feedback during this period. The third regime, occurring after melt onset, is characterized by rapid growth in predictability owing to melt-driven changes in SIM associated with positive ice-albedo feedbacks acting upon the preexisting SIM anomaly.

We find that covariance decompositions computed over other Arctic regions also support this mechanism for the spring predictability barrier (Figure S6). In particular, we find that in all regions of summer SIA variability, the rapid spring increase in SIM-SIA covariance is driven by the melt term. We also find that export-driven mass anomalies provide positive covariance contributions and growth-driven anomalies provide negative contributions in all regions, but there are regional differences in the timing and shapes of these relationships.

3.3. Barrier Evolution Under Climate Change

How will the spring predictability barrier evolve under climate change? Given our proposed mechanism and the observed trend toward earlier melt-onset dates (Bliss & Anderson, 2018; Stroeve et al., 2014), could the barrier shift to an earlier date in a warmer Arctic? We consider this evolution in Figure 4, plotting the covariance decomposition between Laptev Sea SIM and 1 August SIA in different temporal epochs. A 1 August SIA target date is used for this analysis, as both models are nearly September ice free in this region by 2020 but retain August ice until approximately 2040 in CESM and 2060 in FLOR (see Figure S7). We find that both models display qualitatively consistent covariance decompositions across a range of climate mean states, supporting the mechanism identified in the control epoch. Between 1925 and 2050, the ensemble mean melt-onset date shifts earlier by 10 days in CESM and 9 days in FLOR (gray dots in Figure 4). There is a corresponding shift in both melt-based covariance and overall

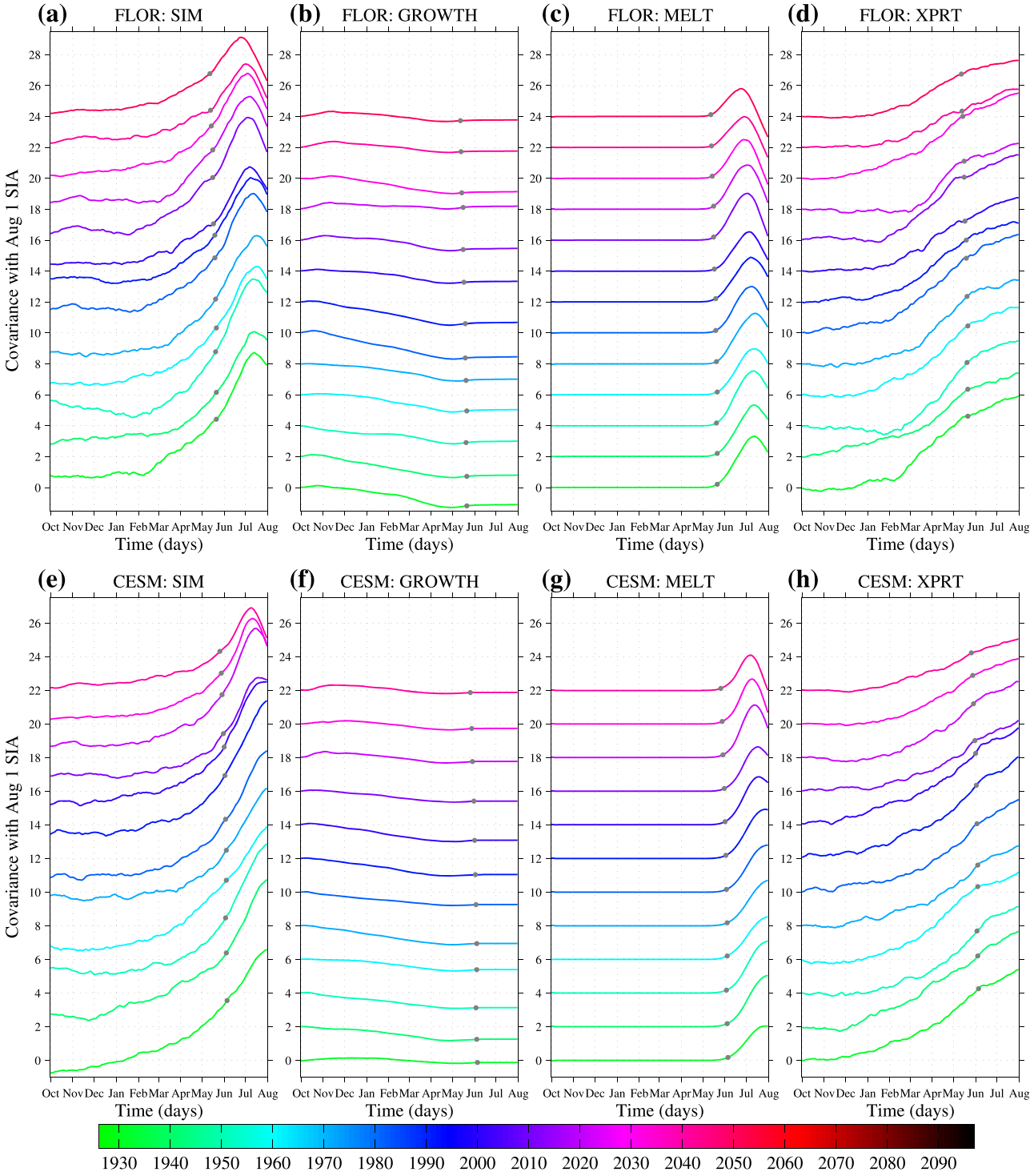

Figure 4. Covariance decompositions between 1 August SIA and earlier SIM in the Laptev Sea in different temporal epochs. Plotted are the full SIM covariance and the contributions from growth, melt, and export in FLOR (a–d) and CESM (e–h). Gray dots indicate the timing of melt onset in each epoch. Covariance values are shown every 10 years starting from 1930 until the models become ice free on 1 August. Each covariance curve has been vertically offset by 2.0 covariance units for visual clarity.

SIM covariance (Figures 4a, 4c, 4e, and 4g). This suggests that the spring predictability barrier will shift earlier under climate change due to earlier melt onset; however, the expected shift is relatively modest and would likely be difficult to detect in current operational prediction systems. We also find that,

starting in roughly 2020, the growth term begins to make positive covariance contributions in October and early November. This is likely due to the trend toward later freeze-up dates and the memory of summer upper-ocean heat content anomalies, which either delay or enhance autumn sea ice growth (Blanchard-Wrigglesworth, Armour, et al., 2011; Cheng et al., 2016).

4. Discussion and Conclusions

We have presented a mechanism for the Arctic sea ice spring predictability barrier—defined as a springtime date such that predictions initialized on or after the date can skillfully predict summer SIA, whereas predictions initialized prior to the date have much lower skill. Based on daily mass budget analyses of the CESM-LE and FLOR-LE, we have quantified the contributions of different processes to SIM-based predictability of summer SIA. We have found that ice export is the dominant driver of regional SIM variability in fall, winter, and spring seasons and that these export-generated variations are partially opposed by the negative ice growth-thickness feedback. Export-driven mass anomalies represent the accumulated effect of synoptic events, which are inherently unpredictable beyond a few weeks. Consequently, summer SIA predictability increases over the winter months, but at a relatively modest rate. This rate begins to increase once the negative feedback from ice growth "turns off" on roughly 1 April. Finally, the barrier timing is characterized by a rapid increase in predictability due to melt-generated SIM anomalies, beginning at the time of melt onset. These melt-driven anomalies act to "lock in" the preexisting export-driven mass anomaly via positive ice-albedo feedbacks, which enhance the mass anomaly. This anomaly persists through the melt season, creating a corresponding late-summer SIA anomaly. We find that the barrier shifts earlier by approximately 10 days in both models between 1925 and 2050 under an RCP8.5 forcing scenario, which is consistent with their trends in melt-onset timing.

The barrier mechanism presented in this study draws upon a number of ingredients presented in earlier work on Arctic sea ice predictability. This mechanism builds upon many previous studies that have identified SIT as the key source of predictability for summer SIA (e.g., Blanchard-Wrigglesworth, Bitz, et al., 2011, 2017; Blockley & Peterson, 2018; Bonan et al., 2019; Bushuk et al., 2017b; Chevallier & Salas, 2012; Collow et al., 2015; Day, Hawkins, et al., 2014; Dirkson et al., 2017; Guemas et al., 2016; Holland et al., 2011, 2019). Earlier work has showed that preconditioning of early summer SIT anomalies via winter and spring ice dynamics is an important source of summer SIA predictability (Babb et al., 2019; Brunette et al., 2019; Itkin & Krumpen, 2017; Krumpen et al., 2013; Williams et al., 2016). Another line of work has demonstrated the importance of melt season ice-albedo feedback processes in predicting September SIA (Cox et al., 2016; Kapsch et al., 2014; Kwok et al., 2018; Landy et al., 2015; Liu et al., 2015; Petty et al., 2017; Schröder et al., 2014; Zhan & Davies, 2017). The predictability barrier mechanism brings these two perspectives together, showing that both dynamic and thermodynamic mechanisms of summer sea ice predictability are essential contributors to the spring barrier. A similar connection between dynamic and thermodynamic predictability has been noted in the earlier work of Williams et al. (2016), Brunette et al. (2019), and Babb et al. (2019).

Bonan et al. (2019) posed the following question: Why is the spring predictability barrier so robust across the diverse set of CMIP5 GCMs? The barrier mechanism suggests that a GCM must have the following essential ingredients to capture barrier-like behavior: (1) a representation of synoptic atmospheric variability in the Arctic; (2) ice dynamics that respond to this wind forcing; (3) ice growth rates that vary inversely with ice thickness; and (4) a representation of the ice-albedo feedback. Vavrus (2013) showed that CMIP5 GCMs are able to simulate strong polar storms with quite high fidelity, suggesting that (1) is satisfied. Additionally, the sea ice dynamic and thermodynamic formulations in CMIP5 have sufficient complexity to capture, at least in a crude sense, Items (2)–(4) (Massonnet et al., 2012). This explains why the spring predictability barrier is robustly captured across CMIP5 models. The barrier mechanism also provides an explanation for why the spring barrier is more sharply defined for regional SIA than pan-Arctic SIA. In particular, since the effects of regional ice dynamics tend to cancel out on the pan-Arctic scale (Blanchard-Wrigglesworth & Bitz, 2014; Tietsche et al., 2014), there is a greater role for longer thermodynamic timescales in pan-Arctic SIA predictability, allowing for skillful pan-Arctic predictions initialized prior to spring.

The spring predictability barrier implies that SIT observations collected past the melt onset date are particularly critical for seasonal predictions of regional summer Arctic sea ice. Crucially, current generation

satellite-based SIT products terminate in mid-April, prior to the melt-onset date, due to algorithmic challenges associated with surface-melt features (Ricker et al., 2014; Tilling et al., 2015). Extending these data as far as possible into the melt season would likely lead to substantial improvements in seasonal prediction skill. Recent observations collected with the IceSat-2 satellite suggest an exciting potential for a new frontier of high-resolution summer SIT data (Kwok et al., 2019), which could enable future sea ice forecasts to achieve their full potential.

Data Availability Statement

The daily NASA team sea ice concentration observations used in this study are available from the National Snow and Ice Data Center website (http://nsidc.org/data/NSIDC-0051/versions/1). The daily PIOMAS sea ice thickness data are available from the Polar Science Center at the University of Washington (http://psc.apl.uw.edu/research/projects/arctic-sea-ice-volume-anomaly/data/model_grid). The CESM-LE data are available for download from the Earth System Grid Federation data portal (http://www.cesm.ucar.edu/projects/community-projects/LENS/data-sets.html). The FLOR-LE sea ice data and data analysis code are available online via Zenodo (https://doi.org/10.5281/zenodo.3862947).

Acknowledgments

We thank two anonymous reviewers for constructive comments. We thank Elisa Mantelli and Gan Zhang for comments on a preliminary version of this manuscript. This research from the Geophysical Fluid Dynamics Laboratory is supported by NOAA's Science Collaboration Program and administered by UCAR's Cooperative Programs for the Advancement of Earth System Science (CPAESS) under Awards NA16NWS4620043 and NA18NWS4620043B. D. B. B. gratefully acknowledges support from the AMS Graduate Fellowship. E. B. W. gratefully acknowledges support from NSF Grant 1751363. We acknowledge the CESM Large Ensemble Community Project, which is supported by the National Science Foundation (NSF). Five of the CESM-LE simulations were produced at the University of Toronto under the supervision of Paul Kushner. We acknowledge computing resources from GFDL's Seasonal-to-Decadal Variability and Predictability Division that were used to produce the FLOR-LE.

References

Babb, D., Landy, J., Barber, D., & Galley, R. (2019). Winter sea ice export from the Beaufort Sea as a preconditioning mechanism for enhanced summer melt: A case study of 2016. *Journal of Geophysical Research: Oceans*, *124*, 6575–6600. https://doi.org/10.1029/2019JC015053

Bitz, C., Holland, M., Weaver, A., & Eby, M. (2001). Simulating the ice-thickness distribution in a coupled climate model. *Journal of Geophysical Research*, *106*(C2), 2441–2463.

Bitz, C. M., & Lipscomb, W. H. (1999). An energy-conserving thermodynamic model of sea ice. *Journal of Geophysical Research*, *104*(C7), 15,669–15,677.

Bitz, C., & Roe, G. (2004). A mechanism for the high rate of sea ice thinning in the Arctic Ocean. *Journal of Climate*, *17*(18), 3623–3632.

Blanchard-Wrigglesworth, E., Bitz, C., & Holland, M. (2011). Influence of initial conditions and climate forcing on predicting Arctic sea ice. *Geophysical Research Letter*, *38*, L18503. https://doi.org/10.1029/2011GL048807

Blanchard-Wrigglesworth, E., Barthélemy, A., Chevallier, M., Cullather, R., Fučkar, N., Massonnet, F., et al. (2017). Multi-model seasonal forecast of Arctic sea-ice: Forecast uncertainty at pan-Arctic and regional scale. *Climate Dynamics*, *49*(4), 1399–1410.

Blanchard-Wrigglesworth, E., & Bitz, C. M. (2014). Characteristics of Arctic sea-ice thickness variability in GCMs. *Journal of Climate*, *27*(21), 8244–8258.

Blanchard-Wrigglesworth, E., Armour, K. C., Bitz, C. M., & DeWeaver, E. (2011). Persistence and inherent predictability of Arctic sea ice in a GCM ensemble and observations. *Journal of Climate*, *24*, 231–250.

Bliss, A. C., & Anderson, M. R. (2018). Arctic sea ice melt onset timing from passive microwave-based and surface air temperature-based methods. *Journal of Geophysical Research: Atmospheres*, *123*, 9063–9080. https://doi.org/10.1029/2018JD028676

Blockley, E. W., & Peterson, K. A. (2018). Improving Met Office seasonal predictions of Arctic sea ice using assimilation of CryoSat-2 thickness. *The Cryosphere*, *12*(11), 3419–3438.

Bonan, D., Bushuk, M., & Winton, M. (2019). A spring barrier for regional predictions of summer Arctic sea ice. *Geophysical Research Letter*, *46*, 5937–5947. https://doi.org/10.1029/2019GL082947

Briegleb, B. P., & Light, B. (2007). A delta-Eddington multiple scattering parameterization for solar radiation in the sea ice component of the Community Climate System Model (Tech. Rep. TN-4721+STR). National Center for Atmospheric Research.

Brunette, C., Tremblay, B., & Newton, R. (2019). Winter coastal divergence as a predictor for the minimum sea ice extent in the Laptev Sea. *Journal of Climate*, *32*(4), 1063–1080.

Bushuk, M., Msadek, R., Winton, M., Vecchi, G., Gudgel, R., Rosati, A., & Yang, X. (2017a). Skillful regional prediction of Arctic sea ice on seasonal timescales. *Geophysical Research Letter*, *44*, 4953–4964. https://doi.org/10.1002/2017GL073155

Bushuk, M., Msadek, R., Winton, M., Vecchi, G., Gudgel, R., Rosati, A., & Yang, X. (2017b). Summer enhancement of Arctic sea-ice volume anoMalies in the September-ice zone. *Journal of Climate*, *30*, 2341–2362.

Bushuk, M., Msadek, R., Winton, M., Vecchi, G., Yang, X., Rosati, A., & Gudgel, R. (2018). Regional Arctic sea-ice prediction: Potential versus operational seasonal forecast skill. *Climate Dynamics*, *52*, 2721–2743.

Cavalieri, D. J., & Parkinson, C. L. (2012). Arctic sea ice variability and trends, 1979–2010. *The Cryosphere*, *6*(4), 881–889. https://doi.org/10.5194/tc-6-881-2012

Cavalieri, D. J., Parkinson, C. L., Gloersen, P., & Zwally, H. J. (1996). Sea ice concentrations from Nimbus-7 SMMR and DMSP SSM/I-SSMIS Passive Microwave Data, Version 1. NASA DAAC at the Natl. Snow and Ice Data Cent. https://doi.org/10.5067/8GQ8LZQVL0VL

Cheng, W., Blanchard-Wrigglesworth, E., Bitz, C. M., Ladd, C., & Stabeno, P. J. (2016). Diagnostic sea ice predictability in the pan-Arctic and US Arctic regional seas. *Geophysical Research Letter*, *43*, 11,688–11,696. https://doi.org/10.1002/2016GL070735

Chevallier, M., & Salas, D. (2012). Mélia The role of sea ice thickness distribution in the Arctic sea ice potential predictability: A diagnostic approach with a coupled GCM. *Journal of Climate*, *25*(8), 3025–3038.

Collow, T. W., Wang, W., Kumar, A., & Zhang, J. (2015). Improving Arctic sea ice prediction using PIOMAS initial sea ice thickness in a coupled ocean–atmosphere model, mon. *Monthly Weather Review*, *143*(11), 4618–4630.

Cox, C. J., Uttal, T., Long, C. N., Shupe, M. D., Stone, R. S., & Starkweather, S. (2016). The role of springtime Arctic clouds in determining autumn sea ice extent. *Journal of Climate*, *29*(18), 6581–6596.

Curry, J. A., Schramm, J. L., & Ebert, E. E. (1995). Sea ice-albedo climate feedback mechanism. *Journal of Climate*, *8*, 240–247.

Day, J., Tietsche, S., & Hawkins, E. (2014). Pan-Arctic and regional sea ice predictability: Initialization month dependence. *Journal of Climate*, *27*(12), 4371–4390.

Day, J., Hawkins, E., & Tietsche, S. (2014). Will Arctic sea ice thickness initialization improve seasonal forecast skill? *Geophysical Research Letter*, *41*, 7566–7575. https://doi.org/10.1002/2014GL061694

Delworth, T. L., Broccoli, A. J., Rosati, A., Stouffer, R. J., Balaji, V., Beesley, J. A., et al. (2006). GFDL'S CM2 global coupled climate models. Part I: Formulation and simulation characteristics. *Journal of Climate*, *19*(5), 643–674.
Dirkson, A., Denis, B., & Merryfield, W. (2019). A multimodel approach for improving seasonal probabilistic forecasts of regional Arctic sea ice. *Geophysical Research Letter*, *46*, 10,844–10,853. https://doi.org/10.1029/2019GL083831
Dirkson, A., Merryfield, W. J., & Monahan, A. (2017). Impacts of sea ice thickness initialization on seasonal Arctic sea ice predictions. *Journal of Climate*, *30*(3), 1001–1017.
Guemas, V., Chevallier, M., Déqué, M., Bellprat, O., & Doblas-Reyes, F. (2016). Impact of sea ice initialisation on sea ice and atmosphere prediction skill on seasonal timescales. *Geophysical Research Letter*, *43*, 3889–3896. https://doi.org/10.1002/2015GL066626
Holland, M. M., Bailey, D. A., Briegleb, B. P., Light, B., & Hunke, E. (2012). Improved sea ice shortwave radiation physics in CCSM4: The impact of melt ponds and aerosols on Arctic sea ice. *Journal of Climate*, *25*(5), 1413–1430.
Holland, M. M., Bailey, D. A., & Vavrus, S. (2011). Inherent sea ice predictability in the rapidly changing Arctic environment of the Community Climate System Model, version 3. *Climate Dynamics*, *36*(7-8), 1239–1253.
Holland, M. M., Landrum, L., Bailey, D., & Vavrus, S. (2019). Changing seasonal predictability of Arctic summer sea ice area in a warming climate. *Journal of Climate*, *32*(16), 4963–4979.
Hunke, E. C., & Dukowicz, J. K. (2002). The elastic–viscous–plastic sea ice dynamics model in general orthogonal curvilinear coordinates on a sphere—Incorporation of metric terms. *Monthly Weather Review*, *130*(7), 1848–1865.
Hunke, E. C., Lipscomb, W. H., Turner, A. K., Jeffery, N., & Elliot, S. (2015). CICE: The Los Alamos sea ice model documentation and software user's manual version 5.1 LA-CC-06-012. t-3 fluid dynamics group Los Alamos National Laboratory 675.
Hunke, E., Lipscomb, W., Turner, A., Jeffery, N., & Elliott, S. (2008). CICE: The Los Alamos sea ice model, documentation and software, version 4.0. Los Alamos National Laboratory Tech. Rep (Tech. rep., LA-CC-06-012).
Hurrell, J. W., Holland, M. M., Gent, P. R., Ghan, S., Kay, J. E., Kushner, P. J., et al. (2013). The Community Earth System model: A framework for collaborative research. *Bulletin of the American Meteorological Society*, *94*(9), 1339–1360.
Itkin, P., & Krumpen, T. (2017). Winter sea ice export from the Laptev Sea preconditions the local summer sea ice cover and fast ice decay. *The Cryosphere*, *11*(5), 2383–2391.
Jung, T., Gordon, N. D., Bauer, P., Bromwich, D. H., Chevallier, M., Day, J. J., et al. (2016). Advancing polar prediction capabilities on daily to seasonal time scales. *Bulletin of the American Meteorological Society*, *97*(9), 1631–1647. https://doi.org/10.1175/BAMS-D-14-00246.1
Kapsch, M.-L., Graversen, R. G., Economou, T., & Tjernström, M. (2014). The importance of spring atmospheric conditions for predictions of the Arctic summer sea ice extent. *Geophysical Research Letter*, *41*, 5288–5296. https://doi.org/10.1002/2014GL060826
Kay, J. E., Deser, C., Phillips, A., Mai, A., Hannay, C., Strand, G., et al. (2015). The Community Earth System Model (CESM) large ensemble project: A community resource for studying climate change in the presence of internal climate variability. *Bulletin of the American Meteorological Society*, *96*(8), 1333–1349.
Keen, A., Blockley, E., Bailey, D., Debernard, J. B., Bushuk, M., Delhaye, S., et al. (2020). An inter-comparison of the mass budget of the Arctic sea ice in CMIP6 models. *The Cryosphere Discussions*, *2020*, 1–39. https://doi.org/10.5194/tc-2019-314
Krumpen, T., Janout, M., Hodges, K., Gerdes, R., Girard-Ardhuin, F., Hölemann, J., & Willmes, S. (2013). Variability and trends in Laptev Sea ice outflow between 1992–2011. *The Cryosphere*, *7*, 1–15.
Kwok, R. (2018). Arctic sea ice thickness, volume, and multiyear ice coverage: L,osses and coupled variability (1958–2018). *Environmental Research Letters*, *13*, 105,005.
Kwok, R., Cunningham, G., & Armitage, T. (2018). Relationship between specular returns in CryoSat-2 data, surface albedo, and Arctic summer minimum ice extent. *Elementa: Science of the Anthropocene*, *6*, 1–10.
Kwok, R., Cunningham, G., Markus, T., Hancock, D., Morison, J. H., Palm, S. P., et al. (2019). The ICESat-2 science team. ATLAS/ICESat-2 L3A Sea Ice Height, Version 2 NASA DAAC at the Natl. Snow and Ice Data Cent. https://doi.org/10.5067/ATLAS/ATL07.002
Landy, J. C., Ehn, J. K., & Barber, D. G. (2015). Albedo feedback enhanced by smoother Arctic sea ice. *Geophysical Research Letter*, *42*, 10,714–10,720. https://doi.org/10.1002/2015GL066712
Lindsay, R., Zhang, J., Schweiger, A., & Steele, M. (2008). Seasonal predictions of ice extent in the Arctic Ocean. *Journal of Geophysical Research*, *113*, C02023. https://doi.org/10.1029/2007JC004259
Liu, J., Song, M., Horton, R. M., & Hu, Y. (2015). Revisiting the potential of melt pond fraction as a predictor for the seasonal Arctic sea ice extent minimum. *Environmental Research Letters*, *10*(5), 054017.
Massonnet, F., Fichefet, T., Goosse, H., Bitz, C. M., Philippon-Berthier, G., Holland, M. M., & Barriat, P.-Y. (2012). Constraining projections of summer Arctic sea ice. *The Cryosphere*, *6*(6), 1383–1394.
Massonnet, F., Vancoppenolle, M., Goosse, H., Docquier, D., Fichefet, T., & Blanchard-Wrigglesworth, E. (2018). Arctic sea-ice change tied to its mean state through thermodynamic processes. *Nature Climate Change*, *8*(7), 599–603.
Meinshausen, M., Smith, S. J., Calvin, K., Daniel, J. S., Kainuma, M., Lamarque, J.-F., et al. (2011). The RCP greenhouse gas concentrations and their extensions from 1765 to 2300. *Climate Change*, *109*(1-2), 213.
Melia, N., Haines, K., Hawkins, E., & Day, J. (2017). Towards seasonal Arctic shipping route predictions. *Environmental Research Letters*, *12*(8), 084005.
Merryfield, W., Lee, W.-S., Wang, W., Chen, M., & Kumar, A. (2013). Multi-system seasonal predictions of Arctic sea ice. *Geophysical Research Letter*, *40*, 1551–1556. https://doi.org/10.1002/grl.50317
Msadek, R., Vecchi, G., Winton, M., & Gudgel, R. (2014). Importance of initial conditions in seasonal predictions of Arctic sea ice extent. *Geophysical Research Letter*, *41*, 5208–5215. https://doi.org/10.1002/2014GL060799
Petty, A. A., Schröder, D., Stroeve, J., Markus, T., Miller, J., Kurtz, N., et al. (2017). Skillful spring forecasts of September Arctic sea ice extent using passive microwave sea ice observations. *Earth's Future*, *5*(2), 254–263. https://doi.org/10.1002/2016EF000495
Preußer, A., Heinemann, G., Willmes, S., & Stephan, P. (2016). Circumpolar polynya regions and ice production in the Arctic: Results from MODIS thermal infrared imagery from 2002/2003 to 2014/2015 with a regional focus on the Laptev Sea. *The Cryosphere*, *10*(6), 3021.
Ricker, R., Hendricks, S., Helm, V., Skourup, H., & Davidson, M. (2014). Sensitivity of CryoSat-2 Arctic sea-ice freeboard and thickness on radar-waveform interpretation. *The Cryosphere*, *8*(4), 1607–1622.
Schröder, D., Feltham, D. L., Flocco, D., & Tsamados, M. (2014). September Arctic sea-ice minimum predicted by spring melt-pond fraction. *Nature Climate Change*, *4*(5), 353–357.
Schweiger, A., Lindsay, R., Zhang, J., Steele, M., Stern, H., & Kwok, R. (2011). Uncertainty in modeled Arctic sea ice volume. *Journal of Geophysical Research*, *116*, C00D06. https://doi.org/10.1029/2011JC007084
Sigmond, M., Fyfe, J., Flato, G., Kharin, V., & Merryfield, W. (2013). Seasonal forecast skill of Arctic sea ice area in a dynamical forecast system. *Geophysical Research Letter*, *40*, 529–534. https://doi.org/10.1002/grl.50129

Stroeve, J., Markus, T., Boisvert, L., Miller, J., & Barrett, A. (2014). Changes in Arctic melt season and implications for sea ice loss. *Geophysical Research Letter*, *41*, 1216–1225. https://doi.org/10.1002/2013GL058951

Thorndike, A. S., Rothrock, D., Maykut, G., & Colony, R. (1975). The thickness distribution of sea ice. *Journal of Geophysical Research*, *80*(33), 4501–4513.

Tietsche, S., Day, J., Guemas, V., Hurlin, W., Keeley, S., Matei, D., et al. (2014). Seasonal to interannual Arctic sea ice predictability in current global climate models. *Geophysical Research Letter*, *41*, 1035–1043. https://doi.org/10.1002/2013GL058755

Tilling, R. L., Ridout, A., Shepherd, A., & Wingham, D. J. (2015). Increased arctic sea ice volume after anomalously low melting in 2013. *Nature Geoscience*, *8*(8), 643–646.

Vavrus, S. J. (2013). Extreme Arctic cyclones in CMIP5 historical simulations. *Geophysical Research Letter*, *40*, 6208–6212. https://doi.org/10.1002/2013GL058161

Vecchi, G. A., Delworth, T., Gudgel, R., Kapnick, S., Rosati, A., Wittenberg, A. T., et al. (2014). On the seasonal forecasting of regional tropical cyclone activity. *Journal of Climate*, *27*(21), 7994–8016.

Walsh, J. E., Stewart, J. S., & Fetterer, F. (2019). Benchmark seasonal prediction skill estimates based on regional indices. *The Cryosphere*, *13*(4), 1073–1088.

Wang, W., Chen, M., & Kumar, A. (2013). Seasonal prediction of Arctic sea ice extent from a coupled dynamical forecast system. *Monthly Weather Review*, *141*(4), 1375–1394.

Wang, X., Key, J., Kwok, R., & Zhang, J. (2016). Comparison of Arctic sea ice thickness from satellites, aircraft, and PIOMAS data. *Remote Sensing*, *8*(9), 713.

Williams, J., Tremblay, B., Newton, R., & Allard, R. (2016). Dynamic preconditioning of the minimum September sea-ice extent. *Journal of Climate*, *29*(16), 5879–5891.

Willmes, S., Adams, S., Schröder, D., & Heinemann, G. (2011). Spatio-temporal variability of polynya dynamics and ice production in the Laptev Sea between the winters of 1979/80 and 2007/08. *Polar Research*, *30*(1), 5971.

Winton, M. (2000). A reformulated three-layer sea ice model. *Journal of Atmospheric and Oceanic Technology*, *17*(4), 525–531.

Yuan, X., Chen, D., Li, C., Wang, L., & Wang, W. (2016). Arctic sea ice seasonal prediction by a linear Markov model. *Journal of Climate*, *29*(22), 8151–8173.

Zhan, Y., & Davies, R. (2017). September Arctic sea ice extent indicated by June reflected solar radiation. *Journal of Geophysical Research: Atmospheres*, *122*, 2194–2202. https://doi.org/10.1002/2016JD025819

Zhang, J., & Rothrock, D. (2003). Modeling global sea ice with a thickness and enthalpy distribution model in generalized curvilinear coordinates. *Monthly Weather Review*, *131*(5), 845–861.